Asian Journal of Chemistry; Vol. 37, No. 7 (2025), 1641-1648

ASIAN JOURNAL OF CHEMISTRY

https://doi.org/10.14233/ajchem.2025.33891

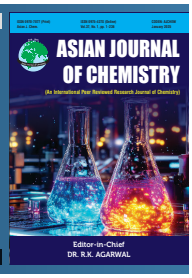

Synthesis of Magnesium/Copper Doped or co-doped ZnO as Photoanode: A Study of Optical and Structural Properties for Enhancing the Photovoltaic Properties of DSSCs

KIRTI HOODA[1], ANSHUL SINGH[1,*], VIRENDER SINGH KUNDU[2] and AMAN KUMAR[3]

[1]Department of Chemistry, Baba Mastnath University, Rohtak-124021, India
[2]Department of Electronic Science, Kurukshetra University, Kurukshetra-136119, India
[3]Department of Physics, Maharishi Markandeshwar Deemed to be University, Mullana-133203, India

*Corresponding author: E-mail: anshul9008@gmail.com

Received: 16 April 2025; *Accepted*: 3 June 2025; *Published online*: 30 June 2025; AJC-22038

Pure ZnO and Cu/Mg co-doped ZnO nanoparticles were synthesized using sol-gel technique. The optical, morphological and structural characteristics of the prepared samples were thoroughly examined. The single-phase hexagonal wurtzite structure, devoid of any impurity phase, was identified by X-ray diffraction data. The effective integration of Cu^{2+}/Mg^{2+} ions into the host ZnO structure is validated by XRD. To examine the morphology of the materials, field emission scanning electron microscopy was utilized. The results showed that the ZnO nanoparticles were highly agglomerated and widely distributed, with a nearly distinct crystalline character. UV-visible spectroscopy was used to analyze the optical characteristics of samples. The electrochemical characteristics of fill factor, open circuit voltage and short circuit current density were determined using J-V characterization. In dye-sensitized solar cell (DSSC), copper ions serve as a barrier layer that prevents electrons from flowing backward, hence reducing recombination. The efficiency of DSSCs improves due to reduced charge recombination. An alternative approach to optimizing photovoltaic performance involves cationic substitution of metal ions, such as Mg^{2+}, in ZnO. This modification not only influences the positioning of the conduction band but also slightly broadens the band gap, contributing to enhanced energy conversion efficiency. The effect of Cu^{2+}/Mg^{2+} doping in a ZnO-based DSSC's efficiency was examined in the current study and the efficiency of Cu^{2+}/Mg^{2+} co-doped ZnO photoanode in DSSCs were measured at 0.8140%, showing an enhancement of approximately 238% compared to the efficiency of pure ZnO-based photoanode utilized in DSSCs. An improved DSSC light harvesting efficiency is supported by all of these findings. This proves that doping ZnO nanoparticles is a good way to boost the appropriate efficiency of a solar cell application.

Keywords: Copper/Magnesium co-doped ZnO nanoparticles, Dye sensitized solar cell, Sol-gel, Photoanode.

INTRODUCTION

The provision of energy plays a crucial role in determining the quality of human life. It is projected that global energy consumption will increase more than three-fold by the end of the century and more than double by the year 2050 [1]. The increasing energy supply will be insufficient to sustainably meet future demands. One of the most pressing challenges facing humanity is the transition to clean energy. However, without the rapid development and deployment of renewable energy sources, this critical issue will remain unresolved, posing a continued threat to global sustainability. Consequently, eco-friendly alternatives like solar and wind energy have become increasingly significant in addressing the rising energy demand.

One clean and practically limitless source of energy is solar. It can be transformed straight into electricity without causing any carbon-emitting pollutants. There is currently a lot of interest in solar energy as a replacement for fossil fuels, which will inevitably run out in the upcoming years. The dye-sensitized solar cells (DSSCs), one of the many solar energy conversion methods, have drawn a lot of interest as a promising technology due to its technical and financial advantages including low material costs, ease of fabrication and potential for large-scale production [2-4]. It comprises a semiconducting metal oxide layer that serves as a substrate for dye adsorption while enabling charge transfer from the dye to the external circuit. To maximize dye loading and enhance charge transport efficiency, the metal oxide layer must exhibit a high surface area and substantial porosity.

To attain high-performance dye-sensitized solar cells (DSSCs), researchers have investigated a range of semiconductor materials for their prospective application as photoanodes. Notable examples of these materials include TiO_2, ZnO, SnO_2, Nb_2O_5 and Zn_2SnO_4 [5-9]. In dye-sensitized solar cells, TiO_2 is commonly employed as the photoanode material, demonstrating efficiencies of up to 12% [5]. The use of TiO_2 as a photoanode does have certain disadvantages, though, including decreased long-term stability, high recombination limiting charge transmission and decreased electron mobility. Existing literature highlights several key advantages of ZnO over TiO_2, including its superior electron mobility (ranging from 205 to 300 cm^2/Vs at 300 K), a wide bandgap of 3.37 eV and a substantial exciton binding energy of 60 meV. Moreover, ZnO exhibits lower toxicity and greater cost-effectiveness, making it a compelling alternative for various optoelectronic and photovoltaic applications [6]. Due to its superior band gap, cost-effectiveness, and simplicity of production, ZnO is considered a state-of-the-art and efficient material. Excellent piezoelectric and pyroelectric qualities are displayed by ZnO, which finds extensive use in solar cells, energy harvesters, electronic devices and the biomedical industry [10-12].

In an effort to develop ZnO a more efficient photoanode material that can replace TiO_2, researchers have tried to enhance its surface shape, particle size and thickness while also adding other components to the structure. However, the creation of a Zn^{2+}/dye agglomeration layer on the ZnO surface is assumed to be the cause of the comparatively low efficiency of ZnO-based DSSCs [13]. A high recombination photogenerated charge carriers in ZnO photoanode, which results in a curtailed efficiency of DSSC. The ZnO structure's poor absorption in the visible region is the main factor limiting its effectiveness in DSSC applications, despite its broad band gap and strong absorption capacity in the ultraviolet light area. Overall performance can be improved by modifying ZnO structures to better use the sun spectrum. With this method, the band gap of these structures is reduced in an effort to boost their absorption efficiency in the visible spectrum, which accounts for around 43% of the total solar irradiation [14]. Enhancing the efficiency of dye-sensitized solar cells (DSSCs) employing ZnO photoanodes remains a critical challenge. Incorporating transition metals into the ZnO crystal lattice is a well-established strategy to modulate its bandgap, thereby enhancing its photoactivity in the visible spectrum [15]. Studies have demonstrated that transition metal-doped ZnO inhibits crystal growth, leading to the formation of smaller nanostructures with an enhanced surface area, which is advantageous for various optoelectronic applications [16,17]. Moreover, doping ZnO with metal ions strengthens its electron transport mechanism and lowers the rate of recombination between its conduction band and the redox electrolyte [18,19].

Much work has been done to increase the ZnO-based photoanodes' surface stability by doping the right materials [20,21] and covering the ZnO with core shells [22,23] to stop Zn-dye aggregates from forming and the injected electron from reacting back with the electrolyte. Due to its broader band gap, magnesium-doped ZnO nanoparticles have been identified as a material for the ZnO barrier layer [24,25]. A slight increase in the band gap can significantly enhance the surface stability of ZnO nanoparticles by incorporating low concentrations of Mg ions into the ZnO lattice. This could enhance the stability of ZnO particles against the acidic dye and reduce the recombination of injected electrons with the electrolyte.

Several techniques employed for the synthesis of nanoparticles include molecular beam epitaxy, metal-organic chemical vapour deposition, plasma-enhanced chemical vapour deposition, sputtering, spray pyrolysis, atomic layer deposition, pulsed laser deposition, electron beam evaporation and sol-gel processes [26]. Compared to the previously described approaches, the sol-gel process offers a number of benefits, including simplicity, affordability and efficiency [27]. To achieve the desired results, a sol-gel spin coating technique makes it easy to modify several parameters, such as the precursor solution concentration, the annealing temperature and the annealing time [28].

The present study investigates the effects of doping or co-doping copper (Cu) and magnesium (Mg) into a ZnO-based photoanode for dye-sensitized solar cells (DSSCs). Throughout the investigation, varying concentrations of Mg and Cu were maintained. To enhance the efficiency of dye-sensitized solar cells (DSSCs), this study presents the first in-depth analysis of the structural, morphological, optical and photovoltaic properties of ZnO doped and co-doped with Mg and Cu. The results reveal that Mg and Cu doping/co-doping significantly improve the charge separation, accelerate charge transport dynamics and extend the absorption spectrum into the ultraviolet and near-infrared regions, which were previously inaccessible. These improvements contribute to an increased efficiency of the investigated dye-sensitized solar cells (DSSCs). By adjusting the dopant concentration, sol-gel nanoparticles were prepared and successfully used as a photoanode.

EXPERIMENTAL

The AR grade chemicals like magnesium nitrate hexahydrate, zinc acetate dihydrate, copper acetate monohydrate, sodium hydroxide, ammonium hydroxide, ethanol, acetone, isopropyl alcohol, Triton X-100, FTO, iodine, potassium iodide and ethylene glycol were procured from Sigma-Aldrich, USA.

Synthesis of nanoparticles: Magnesium nitrate hexahydrate, zinc acetate dihydrate and copper acetate monohydrate were taken as starting materials. Sol-gel technique was used to prepare (i) bare ZnO *i.e.* $Zn_{1.0}O$ Zn-21.949 g (wt.%), (ii) Mg-doped ZnO ($Zn_{0.85}Mg_{0.15}O$) Zn-18.65 g, Mg-3.84 g (wt.%), (iii) Cu doped ZnO ($Zn_{0.85}Cu_{0.15}O$) Zn-18.65 g, Cu-2.99 g and (iv) Cu/Mg co-doped ZnO ($Zn_{0.85}Cu_{0.075}Mg_{0.075}O$) Zn-18.65 g, Cu-1.49 g, Mg-1.92 g (wt.%) nanoparticles. For about 4 h, these materials were dissolved in 100 mL of deionized water and vigorously stirred. Ammonia solution (NH_3) was added dropwise while being continuously stirred at 60 ºC for 1 h or until the pH of the reaction mixture reached 8. The well blended solution turned thicker attaining the consistency of a thick gel after being agitated for an entire hour. The resulting gel was than cleaned utilizing deionized water. Later, the gel was allowed to calcine for about 3 h at 350 ºC. The code and composi-

tion of the synthesized samples are displayed in Table-1. In the first sample bare ZnO nanoparticles were prepared, which were then doped using Mg and Cu at different concentrations.

TABLE-1
SAMPLE CODE AND COMPOSITION OF AS SYNTHESIZED Mg-Cu-ZnO NANOPARTICLES

Sample No.	Sample code	Sample composition
1	ZO	$Zn_{1.0}O$
2	MgZO	$Zn_{0.85}Mg_{0.15}O$
3	CuZO	$Zn_{0.85}Cu_{0.015}O$
4	MgCuZO	$Zn_{0.85}Mg_{0.075}Cu_{0.075}O$

The reaction outlined below governs the synthesis of ZnO nanoparticles produced through the sol-gel method [29]:

$$Zn^{2+} + 2OH^- \longrightarrow Zn(OH) \quad (1)$$

$$Zn(OH)_2 + 2OH^- \longrightarrow Zn(OH)_4^{2-} \quad (2)$$

$$Zn(OH)_4^{2-} \longrightarrow ZnO + H_2O + 2OH^- \quad (3)$$

Construction of dye sensitized solar cells

Dye: Ruthenium N719 dye was chosen since it absorbs visible light and has stable anchoring to the ZnO surface and quick electron injection, making it a good DSSC dye.

Preparation of photoanode utilizing fluorine doped tin oxide (FTO) glass sheets: The photoanodes were prepared using FTO-coated conducting glass sheets washed in an ultrasonic bath with soapy water, distilled water and ethanol. After the cleaning, the FTO coated conducting glass sheets were dried and further used for the preparation of photoanodes. During this procedure, The FTO glass was sectioned into 3 cm × 3 cm pieces and subsequently cleaned using a combination of detergent, acetone and deionized water. These pieces were then placed in a sonicator for about 10 min and dried with a hair-dryer. The process of testing the conducting side of FTO involved using a multimeter to measure its electrical conductivity and then marking an appropriate (1 cm × 1 cm) dimension on it. To ensure perfection, a tape was used to mask the substrate, adhering to the measured dimensions of the photoanode. A homogenous paste was than created by adding an appropriate quantity of powdered sample to the ethanol, which was mixed until a uniform consistency was achieved. To ensure even coverage on the FTO substrate, Triton X-100 was used as a surfactant. The paste was then evenly applied onto the FTO using a Doctor-blade technique. Four working electrodes were simultaneously prepared using this method. The prepared photoanodes were placed in a muffle furnace at a temperature of 400 ºC for 35 min. After 35 min, the photoanodes were immersed in the ruthenium N719 dye.

Preparation of electrolyte: Iodide-triiodide (I^-/I_3^-) was employed as an electrolyte to facilitate the conduction between the counter electrode and the photoanode. Added 0.83 g of KI and 0.127 g of I_2 to 10 mL of ethylene glycol and stirred constantly to obtain a homogeneous mixture. The solution should subsequently be placed in a dark container to shield it from the direct sunlight exposure.

Counter electrode preparation: The conductive side of the FTO was identified using a multimeter, following which a carbon layer was deposited using a graphite pencil. The graphite pencil was carefully placed over the whole surface of the FTO to ensure a consistent and continuous coating.

Assembling of DSSC: Upon completion of the preparation of all components of the DSSC, the photoanode was submerged in a dye solution for duration of 24 h. Subsequently, the photoanode was meticulously rinsed with deionized water and allowed to dry. The DSSC was assembled by applying several drops of electrolyte onto the photoanode, after which the photoanode (FTO side) was firmly affixed to the counter electrode (FTO side) utilising a binding clip. A solar simulator was employed to assess the I-V characteristics of the constructed DSSCs.

Sample characterization: The prepared samples were further examined for their structural, morphological, optical and photovoltaic properties utilizing undermentioned techniques:

XRD: The crystalline structure, grain size and composition of ZnO nanoparticles doped and co-doped using Mg/Cu were examined using a PANalytical X'Pert Pro diffractometer. X-ray diffraction measurements were performed using Cu-$K\alpha$ radiation (λ = 1.54056 Å) at 45 kV and 40 mA to evaluate the crystallographic properties of the samples.

UV-visible spectroscopy: A Perkin Elmer Lambda 650 was used to perform UV-visible spectroscopy in order to assess the absorption properties and ascertain the bandgap of different photoanodes. Tauc plots were used to determine the bandgaps for the doped and undoped samples. The wavelength range in which the UV absorption spectrophotometer operated was 190 nm to 900 nm.

FESEM and EDX: The JEOL JSM-7610FPlus FESEM, a field emission scanning electron microscope, was employed to analyze the surface morphologies of the samples. The energy dispersive X-ray spectrometer (EDX), which is integrated with the field emission scanning electron microscope (FE-SEM) system, was employed to assess the elemental composition of the sample surfaces.

Photoluminescence spectra: The sample was analyzed using photoluminescence spectroscopy to examine its defects, bandgap and deficiencies. Using a Xenon lamp as the excitation source, the photoluminescence spectra of doped or co-doped samples at room temperature using a SHIMADZU RF-530 spectrometer were recorded.

Photovoltaic characterization: Assembled solar cell was examined for measuring the current voltage performance, it was performed in dark using oriel solar simulator AM1.5, 100 mW/cm^2, Oriel Sol3A, Newport, Keithley 2400). The photovoltaic current density (J)-voltage (V) was characterized.

RESULTS AND DISCUSSION

XRD analysis: The crystallinity and the particle sizes of ZnO, ZnMgO, ZnCuO and ZnMgCuO nanoparticles were analyzed by the XRD method. Fig. 1 shows the X-ray diffraction patterns of co-doped, Mg/Cu-doped and bare ZnO nanoparticles on an FTO substrate. The graphic indicates that the inclusion of Mg^{2+}/Cu^{2+} using JCPDS card no. 36-1451 [30], which confi-

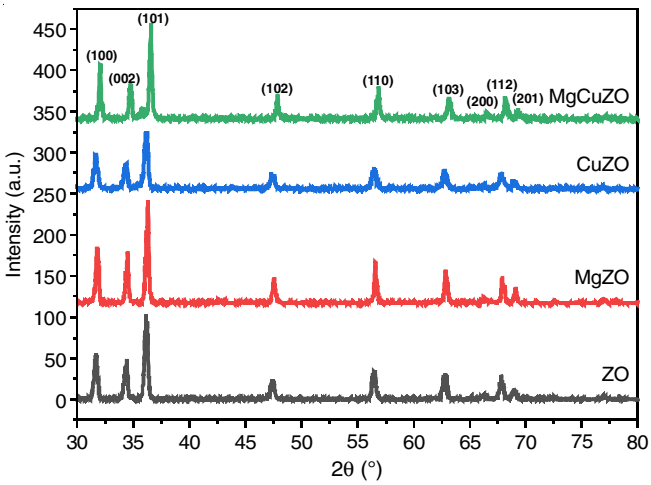

Fig. 1. X-ray diffraction pattern of as synthesized nanoparticles

rmed that the polycrystalline films consist of hexagonal wurtzite structure with no additional phases.

A high level of crystallinity is indicated by the nine sharp and intense ZnO peaks found in all samples ((100), (002), (101), (102), (110), (103), (200), (112) and (201). The XRD spectrum shows no peaks for Cu or Mg ions, indicating that the addition of Cu^{2+} ions has no effect on the hexagonal wurtzite structure [31].

The size of the crystallites in the synthesized particles was ascertained through the application of the Debye-Scherrer's equation, which employs the line broadening (full-width at half-maximum, FWHM) of the (101) diffraction peak [32].

$$D = \frac{0.94\lambda}{\beta\cos\theta} \quad (4)$$

where θ is the Bragg angle (°); β is the full half maximum, FWHM (rad); λ is the wavelength and D is the crystallite size (nm).

Furthermore, using Bragg's rule [33,34], a number of other parameters, such as d-spacing and lattice strain, were determined using the obtained XRD data and are reported in Table-2.

$$\text{Lattice strain } (\varepsilon) = \frac{\beta}{4\tan\theta} \quad (5)$$

$$\text{d-spacing } (d) = \frac{n\lambda}{2\sin\theta} \quad (6)$$

where FWHM and θ have same value mentioned above.

The synthesized samples ZO, MgZO, CuZO and MgCuZO have crystallite sizes of 18.174 nm, 22.964 nm, 18.174 nm and 31.349 nm, respectively. When compared to the bare sample, the increased crystallite size indicates that the atoms are more organized in their orientation.

UV-vis spectral studies: UV-visible spectroscopy was used to analyze the absorbance and band gap of bare ZnO, ZnO nanoparticles doped with Mg^{2+} or Cu^{2+} and those co-doped with both elements in the wavelength range of 300–800 nm. When compared to pure ZnO, it is also evident that the absorption peaks of Mg-doped ZnO move toward a shorter wavelength. When magnesium is doped, the absorption moves to short wavelengths, suggesting a wider band gap. This is due to the fact that Mg doping increases the concentration of free carriers, hence improving absorption. Consequently, a uniform substitution of magnesium for zinc within the lattice induces a blue shift.

The inclusion of magnesium hardly minimally alters the visible spectrum absorption properties of hierarchical ZnO nanostructures. The shift of the absorption edge toward longer wavelengths is caused by a number of causes, including changes in particle size, average crystallite size and oxygen shortage. The overlapping of all spectra at 390 nm indicates that the introduction of Cu^{2+} ions does not impact the light absorption capability of pristine ZnO (Fig. 2). Moreover, pure ZnO exhibits no absorption in the visible spectrum.

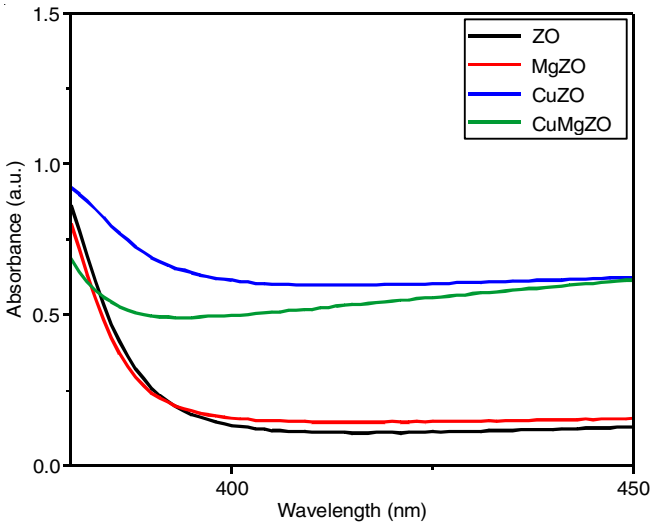

Fig. 2. Optical absorbance spectra of as studied samples

Tauc plot was used to evaluate the band gap energy for the prepared sample [35].

$$(\alpha h\nu) = C(h\nu - E_g)^n \quad (7)$$

where n is equal to 1/2, 3/2, 2 and 3 for transitions that are directly permitted, those that are directly prohibited and those that are allowed indirectly; h = Planck's constant; C = proportionality constant, ν = incoming light frequency; α = absorption coefficient; E_g = optical bandgap energy. Fig. 3 shows the

TABLE-2
CALCULATED/OBSERVED STRUCTURAL PARAMETERS FROM XRD

Sample composition	Diffraction angle* (2θ)	FWHM*	Crystallite size* (nm)	Lattice strain* (Є)	d-Spacing*
$Zn_{1.0}O$	36.1179	0.48	18.174	0.0064	2.484
$Zn_{0.85}Mg_{0.15}O$	36.227	0.38	22.964	0.0050	2.477
$Zn_{0.85}Cu_{0.15}O$	36.1052	0.48	18.174	0.0064	2.485
$Zn_{0.85}Cu_{0.075}Mg_{0.075}O$	36.5219	0.57	31.349	0.0036	2.458

*Parameters corresponding peaks of 100% relative intensities, cooperating well with Fig. 1.

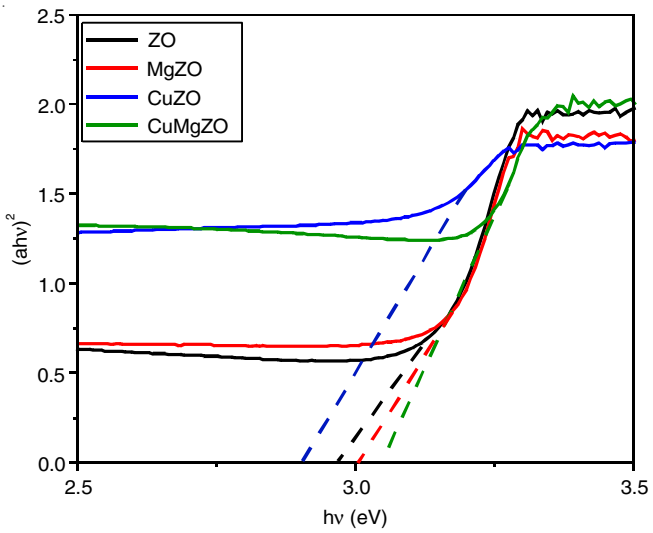

Fig. 3. Tauc plot of various prepared samples

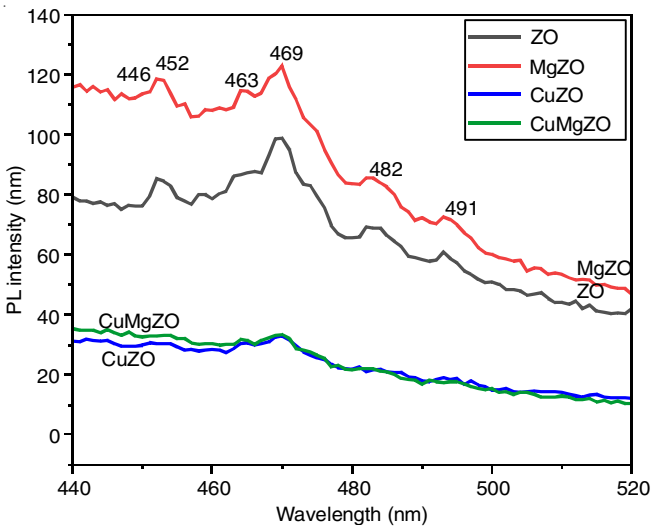

Fig. 4. PL spectra of ZnO doped and co-doped Mg or Cu

observed optical band gap (E_g) values, which are 2.96 eV, 3.01 eV, 2.90 eV and 3.04 eV. Doping ZnO with magnesium results in an increase in the bandgap. This enhancement occurs due to the elevated concentration of free carriers introduced by magnesium doping, which in turn enhances absorption. Whereas there was a slight decrease in bandgap when doped with Cu, which is due to the formation of intermediate states due to Cu loading [36]. These transitional states enhance the photoabsorbance spectrum by facilitating the migration of photoelectrons from lower energy levels in the valence band to the conduction band. Consequently, the bandgap is notably reduced from 2.96 eV to 2.90 eV due to this bandgap tuning, enabling electrons to transition to an excited state with lower energy levels [37].

Photoluminescence studies: All samples were irradiated at a wavelength of 325 nm using xenon light at ambient temperature. Photoluminescence studies were conducted to examine the effects of Cu^{2+}/Mg^{2+} doping and co-doping in ZnO nanoparticles. Fig. 4 presents the photoluminescence (PL) spectra for all the prepared samples over the wavelength range from ultraviolet (UV) to visible light (440-520 nm). Electron-hole pairs associated with intrinsic flaws in the ZnO structure recombine to produce the visible emission. The band structure and energy levels linked to the ZnO defects were analyzed in order to investigate the sources of the emission peaks. Defects including oxygen antisite, zinc vacancy, zinc interstitial and oxygen interstitial are noted. Interstitial oxygen, interstitial zinc, or transitions linked to defects (interface traps) at the grain boundaries and the valence band could be the cause of the emission peaks seen at 446 and 463 nm [38].

The integration of Mg inside the ZnO crystal lattice results in the distortion of the lattice. Such deformation results in enlarged band gap because the Bohr radius of Mg is smaller than Zn. Impurities cause a higher population of carriers to fill the conduction band edge, increasing electrical conductivity in ZnO while optically translocated band-to-band transitions occur at a higher energy, which is referred to as the Burstein-Moss effect. One notable blue emission at 469 nm relates to zinc vacancies (V_{Zn}) within the ZnO lattice [39]. Furthermore, zinc interstitials (Z_{Ni}) in the ZnO structure are responsible for the violet-blue light emission at 452 nm. Furthermore, a relationship is found between the presence of oxygen vacancies (V_o) in the ZnO crystal lattice and the characteristic blue-green light emission that peaks at 482 nm. The strong emission bands show that the photogenerated electron-hole pairs are recombining at a rapid pace. Also, at 452 nm, zinc interstitials (Z_{Ni}) within the ZnO structure emit violet-blue light. Moreover, we discovered a relationship between the presence of oxygen vacancies (V_o) in the ZnO crystal lattice and the characteristic blue-green light emission that peaks at 482 nm. The strong emission bands show that the photogenerated electron-hole pairs are recombining at a rapid pace. The recombination processes were reduced when the sample was co-doped with Mg and Cu, as illustrated in Fig. 4. Consequently, the co-doped sample exhibits lower recombination rates compared to the bare ZnO.

FESEM-EDX studies: Fig. 5 shows the surface morphology and FESEM images of Mg/Cu ZnO nanoparticles in panels (a)-(d) that are bare, doped and co-doped. It is clearly observed that the samples maintain a consistent hexagonal morphology and exhibit a uniform distribution. FESEM images demonstrate that the doping and co-doping of Mg^{2+} and Cu^{2+} do not alter the morphology of ZnO nanoparticles. Nevertheless, there is a significant reduction in the grain size, especially in the co-doped samples.

Fig. 6 shows the EDX spectra of the Cu^{2+}/Mg^{2+} doped and co-doped ZnO nanoparticles, which showed the dopants' composition in the host ZnO. The bare ZnO exhibits peak values for Zn and O at atomic percentages of 45.82% and 54.18%, respectively. When ZnO was doped Mg, the EDX revealed peaks corresponding to Mg, Zn and oxygen (O), with their respective atomic percentages measured at 8.83%, 34.12% and 57.05%. Fig. 6c illustrates the EDX spectrum of Cu-doped ZnO, demonstrating peaks for Cu, Zn and O, with their respective atomic percentages recorded at 4.64%, 42.01% and 53.35%. When ZnO was co-doped with both Mg and Cu, as shown in Fig. 6d, the EDX spectrum reveals additional peaks

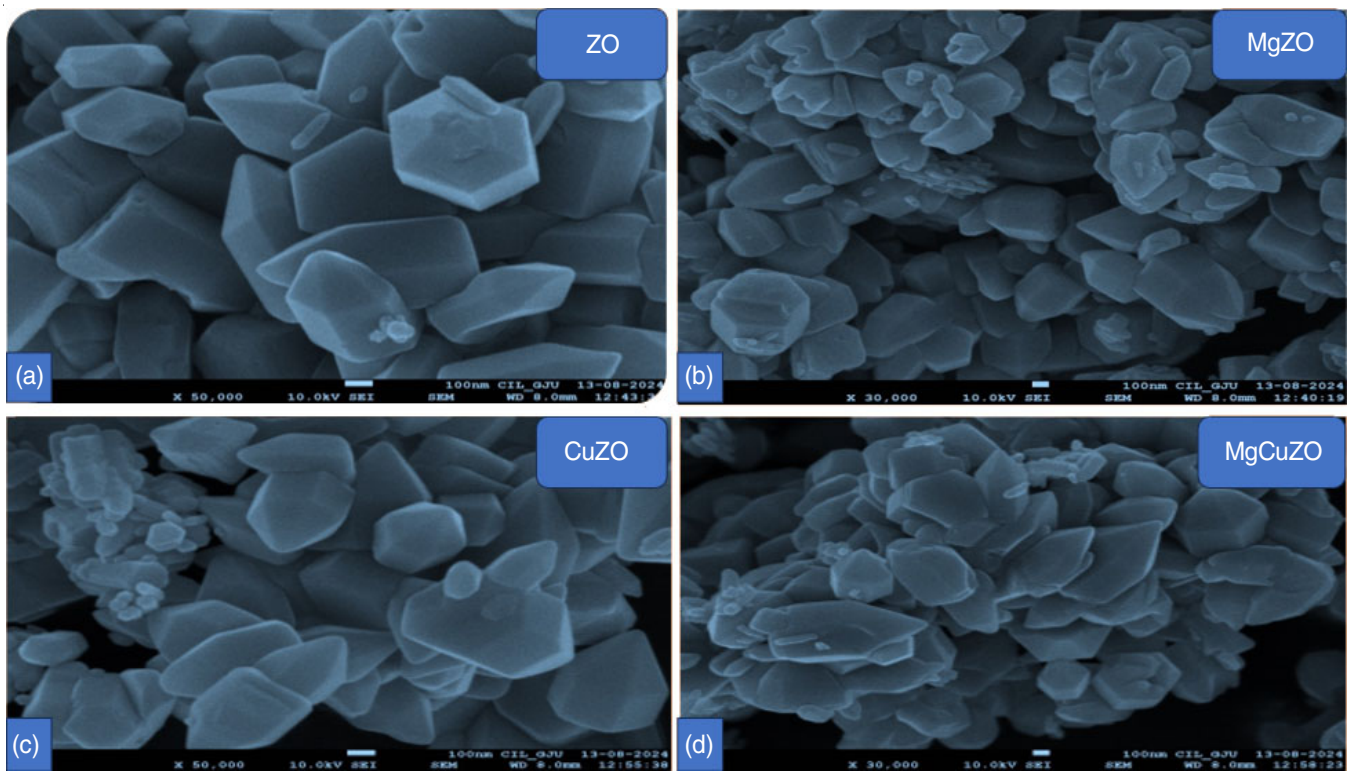

Fig. 5. FESEM images of samples (a) ZO (b) MgZO (c) CuZO and (d) MgCuZO

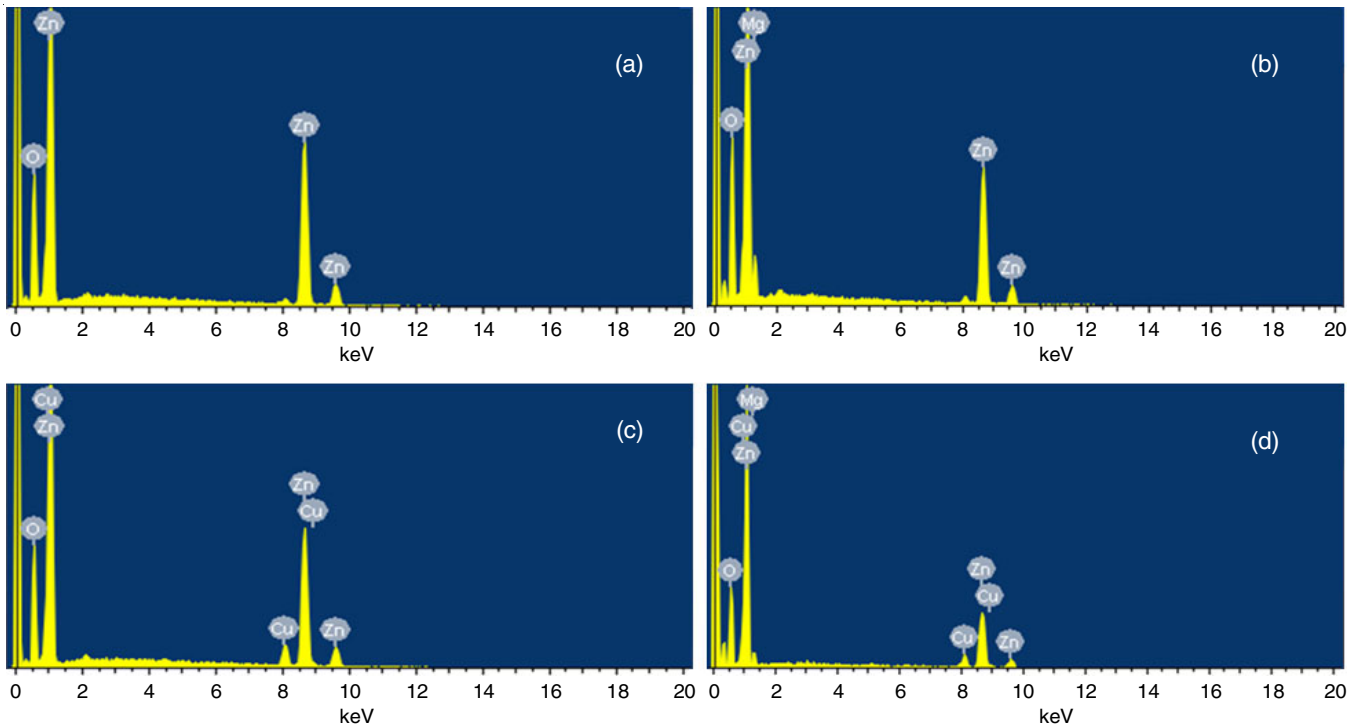

Fig. 6. EDX images of samples ZO, MgZO, CuZO and MgCuZO

corresponding to Mg, Cu, Zn and O, with their respective atomic percentages recorded at 5.65%, 4.06%, 29.97% and 60.32%. Furthermore, XRD analysis shows that neither Cu^{2+}/Mg^{2+}-doped nor Cu-doped ZnO exhibit any diffraction peaks related to impurities like MgO or CuO, demonstrating the successful integration of dopants within the ZnO matrix.

Photovoltaic characterization: In order to investigate the performance variations caused by Cu^{2+}/Mg^{2+} doping and co-doping, ZnO and doped photoanodes (ZO, MgZO, CuZO and MgCuZO) were assembled into DSSCs. Under AM 1.5, 100 mW/cm^2 light irradiation, the performance of these four photoanode series was tested and presented in Fig. 7, with

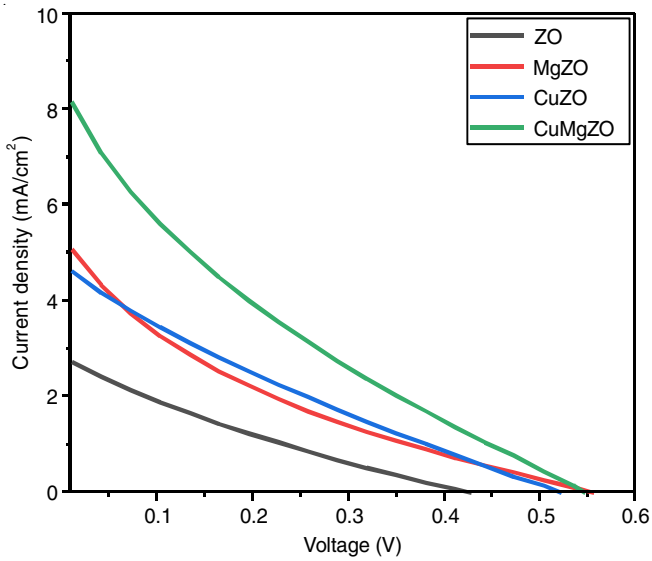

Fig. 7. J-V curve of (ZO, MgZO, CuZO and MgCuZO) photoanode based DSSC

comprehensive characteristics listed in Table-3. The fill factor (FF) and efficiency (η) of dye-sensitized solar cells (DSSCs) were ascertained through the application of the following formulas:

$$FF = \frac{J_{max} \times V_{max}}{J_{sc} \times V_{oc}} \quad (8)$$

$$\eta = \frac{(J_{sc} \times V_{oc} \times FF)}{P_{in}} \quad (9)$$

TABLE-3
A RANGE OF PHOTOVOLTAIC CHARACTERISTICS FOR EACH MANUFACTURED DSSC

Sample	J_{sc} (mA/cm^2)	V_{oc} (V)	FF	Efficiency
ZO	2.887	0.422	19.69	0.2405
MgZO	5.571	0.550	14.44	0.4435
CuZO	4.888	0.514	20.31	0.5108
CuMgZO	9.827	0.541	15.29	0.8140

Based on the recorded J-V curve, the open-circuit voltage (V_{oc}) and short-circuit current density (J_{sc}) were determined. The bare ZnO photoanode based DSSC exhibits V_{oc}, J_{sc}, fill factors and efficiency (η) values of 0.422V, 2.887 mA/cm^2, 19.69 and 0.2405% respectively. In case of Mg doped ZnO based DSSC, the photovoltaic parameters of V_{oc} and J_{sc} increases to 0.550V and 5.571 mA/cm^2, respectively, resulting in an increased η value of 0.4435%. Similarly, Cu doped ZnO based DSSC leads to an increase in the values of V_{oc} and J_{sc} to 0.514V and 4.888 mA/cm^2, respectively, resulting in an increased η value of 0.5108%. Furthermore, Cu^{2+} and Mg^{2+} co-doped ZnO photoanode based DSSC shows enhancement of the photovoltaic parameters, with the values of V_{oc} and J_{sc} escalating to 0.541V and 9.827 mA/cm^2, respectively. This results in an increased η value of 0.8140% as listed in Table-3.

The enhanced efficiency of co-doped solar cells can be attributed to the formation of dopant-induced trap states near the conduction band of the ZnO nanostructure. These trap states promote rapid charge transfer and facilitate the movement of low-energy electrons. Consequently, the doped structures exhibit improved photon absorption and enhanced charge separation, which mitigates the recombination of electron-hole pairs (excitons), thereby improving photoconversion efficiency [40]. After doping, a significant enhancement in the open circuit voltage levels was also observed. The difference in energy between the semiconductor material's Fermi level and the potential of the redox pair in the electrolyte plays a crucial role in determining the open circuit voltage of dye-sensitized solar cells (DSSCs) [41]. The confedration of Cu^{2+} ions into the ZnO hexagonal wurtzite structure plays a pivotal role in enhancing the open-circuit voltage by causing an upward shift in the Fermi energy level, moving it closer to the conduction band edge [42]. Consequently, the co-doped sample surpasses the limitations associated with bare ZnO, demonstrating the maximum efficiency increase of 238% compared to bare ZnO.

Conclusion

This investigation employed the sol-gel method to effectively synthesize Cu^{2+} and Mg^{2+} doped as well as co-doped ZnO nanoparticles. Characterization techniques including EDX, XRD, UV-visible and photoluminescence, demonstrate that Cu^{2+} and Mg^{2+} have been successfully incorporated into the ZnO nanoparticle lattice. Due to the effective integration of the doping ions, the XRD analysis did not exhibit distinct diffraction peaks associated with the metal oxide phases of Cu^{2+} and Mg^{2+}. The UV-visible spectrum demonstrates that the integration of magnesium into zinc oxide (ZnO) leads to a blue shift in the absorption edge and an augmentation of the band gap energy. The measured band gap energies for the samples ZO, MgZO, CuZO and MgCuZO were found to be 2.96 eV, 3.01 eV, 2.90 eV and 3.04 eV, respectively. Photoluminescence (PL) spectroscopy further demonstrates that the introduction of copper ions into ZnO diminishes the recombination of photogenerated electron-hole pairs. FESEM, further confirms the hexagonal wurtzite structure of the prepared nanoparticles while doping and co-doping does not show any influence on the shape of the particles. In contrast to bare ZnO-based DSSC, the solar conversion efficiency of DSSC employing Cu^{2+}/Mg^{2+} co-doped ZnO was found to be 0.8140%, indicating a significant improvement of 238%. The increased efficiency is due to two aspects. Initially, the transition metal ion (Cu) functions as a blocking layer, inhibiting the recombination of electrons by preventing their backflow, thereby significantly reducing recombination rates and enhancing the efficiency of the DSSC. Additionally, the cationic substitution of metal ions (Mg^{2+}) in ZnO has emerged as an effective strategy for modifying the conduction band position, while simultaneously causing a slight increase in the band gap, thereby improving the photovoltaic performance.

ACKNOWLEDGEMENTS

The author expresses sincere gratitude to the Department of Electronic Science, Kurukshetra University, Kurukshetra, India for accessing the essential instrumentation and facilities.

CONFLICT OF INTEREST

The authors declare that there is no conflict of interests regarding the publication of this article.

REFERENCES

1. B.J. van Ruijven, E. De Cian and I.S. Wing, *Nat. Commun.*, **10**, 2762 (2019); https://doi.org/10.1038/s41467-019-10399-3
2. D. Tekin, H. Kiziltas and H. Ungan, *J. Mol. Liq.*, **306**, 112905 (2020); https://doi.org/10.1016/j.molliq.2020.112905
3. F. Machda, T. Ogawa, H. Okumura and K.N. Ishihara, *Phys. Status Solidi., A Appl. Mater. Sci.*, **217**, 1900519 (2020); https://doi.org/10.1002/pssa.201900519
4. P.F. Ji, Y. Li, F.Q. Zhou, Y.L. Song and H.C. Huang, *Mater. Lett.*, **262**, 127028 (2020); https://doi.org/10.1016/j.matlet.2019.127028
5. M.K. Nazeeruddin, E. Baranoff and M. Grätzel, *Sol. Energy*, **85**, 1172 (2011); https://doi.org/10.1016/j.solener.2011.01.018
6. S. Borbón, S. Lugo, D. Pourjafari, N. Pineda Aguilar, G. Oskam and I. López, *ACS Omega*, **5**, 10977 (2020); https://doi.org/10.1021/acsomega.0c00794
7. H. Kim and A. Pique, *Appl. Phys. Lett.*, **84**, 218 (2004); https://doi.org/10.1063/1.1639515
8. A.M. Awwad, M.W. Amer and M.M. Al-Aqarbeh, *Chem. Int.*, **6**, 168 (2020); https://doi.org/10.5281/zenodo.3597558
9. O. Igwe and F. Nwamezie, *Chem. Int.*, **4**, 60 (2018).
10. K.H. Kim, K. Utashiro, Y. Abe and M. Kawamura, *Materials*, **7**, 2522 (2014); https://doi.org/10.3390/ma7042522
11. B. Ali, M.W. Ashraf and S. Tayyaba, *Energies*, **12**, 807 (2019); https://doi.org/10.3390/en12050807
12. M.K. Basher, M.K. Hossain, R. Afaz, S. Tayyaba, M.A.R. Akand, M.T. Rahman and N.M. Eman, *Results Phys.*, **10**, 205 (2018); https://doi.org/10.1016/j.rinp.2018.05.038
13. K. Keis, J. Lindgren, S.-E. Lindquist and A. Hagfeldt, *Langmuir*, **16**, 4688 (2000); https://doi.org/10.1021/la9912702
14. B. Abebe, N.K. Gupta and D. Tsegaye, *RSC Adv.*, **14**, 17338 (2024); https://doi.org/10.1039/D4RA02568G
15. S. Rehman, R. Ullah, A.M. Butt and N.D. Gohar, *J. Hazard. Mater.*, **170**, 560 (2009); https://doi.org/10.1016/j.jhazmat.2009.05.064
16. Y. Peng, S. Qin, W.-S. Wang and A.-W. Xu, *CrystEngComm*, **15**, 6518 (2013); https://doi.org/10.1039/c3ce40798e
17. K.C. Barick, S. Singh, M. Aslam and D. Bahadur, *Micropor. Mesopor. Mater.*, **134**, 195 (2010); https://doi.org/10.1016/j.micromeso.2010.05.026
18. A.M. Toufiq, R. Hussain, A. Shah, A. Mahmood, A. Rehman, A. Khan and S. Rahman, *Physica B*, **604**, 412731 (2021); https://doi.org/10.1016/j.physb.2020.412731
19. E. Akman, *J. Mol. Liq.*, **317**, 114223 (2020); https://doi.org/10.1016/j.molliq.2020.114223
20. Q. Zhang, C.S. Dandeneau, S. Candelaria, D. Liu, B.B. Garcia, X. Zhou, Y.H. Jeong and G. Cao, *Chem. Mater.*, **22**, 2427 (2010); https://doi.org/10.1021/cm9009942
21. A. de Souza Gonçalves, M.R. Davolos, N. Masaki, S. Yanagida, J.R. Durrant, A. Morandeira, J.N. Freitas and A.F. Nogueira, *Dalton Trans.*, **11**, 1487 (2008); https://doi.org/10.1039/b716724e
22. Y.J. Shin, J.H. Lee, J.-H. Park and N.-G. Park, *Chem. Lett.*, **36**, 1506 (2007); https://doi.org/10.1246/cl.2007.1506
23. K. Prabakar, M. Son, W.-Y. Kim and H. Kim, *Mater. Chem. Phys.*, **125**, 12 (2011); https://doi.org/10.1016/j.matchemphys.2010.09.028
24. A. Ohtomo, K. Tamura, M. Kawasaki, T. Makino, Y. Segawa, Z.K. Tang, G.K.L. Wong, Y. Matsumoto and H. Koinuma, *Appl. Phys. Lett.*, **77**, 2204 (2000); https://doi.org/10.1063/1.1315340
25. A. Ohtomo, M. Kawasaki, T. Koida, K. Masubuchi, H. Koinuma, Y. Sakurai, Y. Yoshida, T. Yasuda and Y. Segawa, *Appl. Phys. Lett.*, **72**, 2466 (1998); https://doi.org/10.1063/1.121384
26. A. Jilani, M. Abdel-wahab and A. Hammad, eds.: N. Nikitenkov, Advance Deposition Techniques for Thin Film and Coating, In: Modern Technologies for Creating the Thin-film Systems and Coatings, Chap. 8, pp. 137-143, IntechOpen (2017).
27. F. Aslan, A. Tumbul, A. Göktas, R. Budakoglu and I.H. Mutlu, *J. Sol-Gel Sci. Technol.*, **80**, 389 (2016); https://doi.org/10.1007/s10971-016-4131-z
28. M.N.H. Mia, M.F. Pervez, M.K. Hossain, M. Reefaz-Rahman, M.J. Uddin, M.A. Al Mashud, H.K. Ghosh and M. Hoq, *Results Phys.*, **7**, 2683 (2017); https://doi.org/10.1016/j.rinp.2017.07.047
29. V. Cauda, D. Pugliese, N. Garino, A. Sacco, S. Bianco, F. Bella, A. Lamberti and C. Gerbaldi, *Energy*, **65**, 639 (2014); https://doi.org/10.1016/j.energy.2013.12.025
30. N.S. Gultom, H. Abdullah and D.-H. Kuo, *Appl. Catal. B*, **272**, 118985 (2020); https://doi.org/10.1016/j.apcatb.2020.118985
31. H. Esgin, Y. Caglar and M. Caglar, *J. Alloys Compd.*, **890**, 161848 (2021); https://doi.org/10.1016/j.jallcom.2021.161848
32. M. Mujahid and O.A. Al-Hartomy, *Mater. Res. Innov.*, **27**, 194 (2023); https://doi.org/10.1080/14328917.2022.2113270
33. M. Amjad, M.I. Khan, N. Alwadai, M. Irfan, Ikram-ul-Haq, H. Albalawi, A.H. Almuqrin, M.M. Almoneef and M. Iqbal, *Nanomaterials*, **12**, 1057 (2022); https://doi.org/10.3390/nano12071057
34. J. Chauhan, N. Srivastav, A. Dugaya and D. Pandey, *MOJ Polym. Sci.*, **1**, 26 (2017).
35. B.D. Viezbicke, S. Patel, B.E. Davis and D.P. Birnie III, *Phys. Status Solidi, B Basic Res.*, **252**, 1700 (2015); https://doi.org/10.1002/pssb.201552007
36. R. Mohan, K. Krishnamoorthy and S.-J. Kim, *Solid State Commun.*, **152**, 375 (2012); https://doi.org/10.1016/j.ssc.2011.12.008
37. K.H. Lee, R. Farheen, Z. Arshad, M. Ali, H. Hassan, M. Alshareef, A.Dahshan and U. Khalid, *RSC Adv.*, **14**, 15391 (2024); https://doi.org/10.1039/D4RA01544D
38. Y.Q. Wang, J. Yang, Y.C. Li, T.T. Jiang, J.Y. Chen and J.X. Wang, *Mater. Chem. Phys.*, **153**, 266 (2015); https://doi.org/10.1016/j.matchemphys.2015.01.013
39. C.P. Dietrich, M. Brandt, M. Lange, J. Kupper, T. Böntgen, H. von Wenckstern and M. Grundmann, *J. Appl. Phys.*, **109**, 013712 (2011); https://doi.org/10.1063/1.3530610
40. A. Das, R.R. Wary and R.G. Nair, *Solid State Sci.*, **104**, 106290 (2020); https://doi.org/10.1016/j.solidstatesciences.2020.106290
41. A. Hagfeldt, G. Boschloo, L. Sun, L. Kloo and H. Pettersson, *Chem. Rev.*, **110**, 6595 (2010); https://doi.org/10.1021/cr900356p
42. K.R. Aneesiya and C. Louis, *J. Alloys Compd.*, **829**, 154497 (2020); https://doi.org/10.1016/j.jallcom.2020.154497